Energy & Environmental Science

Accepted Manuscript

ROYAL SOCIETY OF CHEMISTRY

www.rsc.org/ees

Quantification of spatial inhomogeneity in perovskite solar cells by hyperspectral luminescence imaging

Gilbert El-Hajje,[a,b] Cristina Momblona,[c] Lidón Gil-Escrig,[c] Jorge Ávila,[c] Thomas Guillemot,[b] Jean-François Guillemoles,[b,d] Michele Sessolo,[c] Henk J. Bolink*[c] and Laurent Lombez*[b]

[a] EDF R&D, 6 quai Watier, 78400 Chatou, France

[b] Institute of Research and Development on Photovoltaic Energy (IRDEP), UMR 7174 CNRS-EDF- Chimie ParisTech, 6 quai Watier, 78400 Chatou, France. E-mail: laurent.lombez@chimie-paristech.fr

[c] Instituto de Ciencia Molecular, Universidad de Valencia, C/ Catedrático J. Beltrán 2, 46980 Paterna, Spain. E-mail: henk.bolink@uv.es

[d] NextPV, CNRS-RCAST joint lab, Tokyo University, Tokyo, 4-6-1 Komaba, Meguro-ku 153-8904, Japan

Photovoltaic devices based on hybrid organic-inorganic perovskites have attracted great attention due to the rapid evolution of their power conversion efficiencies.[1-12] By far the most efficient architectures have been prepared using a solution processed perovskite absorber, yet efficient solar cells using an evaporated perovskite layer have also been demonstrated.[13-15] It has become clear that not necessarily the preparation method, but the perovskite grain size has a strong effect on the overall performance of the solar cells.[16] Indeed carrier diffusion length can be drastically enhanced to over 100 µm when single crystals are obtained, thanks to a reduction in the density of trap states.[17, 18] Even polycrystalline hybrid perovskite semiconductors are characterized by large and balanced charge diffusion lengths,[19, 20] consequence of the very low non-radiative recombination rates.[21, 22] In an ideal case, charge recombination in a photovoltaic material should be purely radiative, since the same transitions involved in photoluminescence (PL) and electroluminescence (EL) are also responsible for light absorption. Recently, it was shown independently by two groups that perovskite solar cells obey the reciprocity relation as formulated by Rau,[23] which describes the equilibrium between absorption and emission of a single direct band gap semiconductor. Such relation implies that one can predict the photovoltage by measuring the external quantum efficiency (EQE) for EL and from the photocurrent generation efficiency.[24, 25] The radiative efficiency for perovskite solar cells was found to be higher compared to inorganic materials such as amorphous silicon or cadmium telluride, and only slightly lower compared to Cu(In,Ga)Se_2 (CIGS) solar cells.[24] This is one of the reasons behind the generally high open circuit voltage (V_{oc}) observed in methylammonium lead iodide ($MAPbI_3$) based cells (1.0-1.1 V), in view of its bandgap of approximately 1.6 eV. Recently, by correlating confocal microscopy with scanning electron microscopy, the spatial variation of the photoluminescence (PL) intensity and lifetime, over different grain size and boundaries, have been reported.[26] Interestingly, substantial inhomogeneity in the PL mapping was observed, meaning that even efficient perovskite solar cells still contain regions with non-radiative recombination. In another study, the spatially resolved electronic excited-state dynamics have been observed by means of femtosecond transient absorption spectroscopy coupled to an optical microscope.[27] The excited state relaxation was found to be very dependent on the location in the device, hence confirming the presence of substantial inhomogeneity over a large length scale. Very recently, EL and PL images where shown to have a good potential for studying spatial inhomogeneities at a millimeter scale, where local series resistance can fluctuates.[28] These and other recent investigations[29-34] have highlighted the need for a spatial resolved analysis of the physical properties governing the photovoltaic behavior of perovskite solar cells. In particular, the correlation between the spatial variation of a certain physical quantity and the materials morphology will help identifying strategies to improve the overall device performance.

Hyperspectral imaging of luminescence is a novel technique that offers spectrally resolved PL and EL maps of semiconductor devices, and has been recently applied in the characterization of GaAs,[35, 36] silicon,[37, 38] Cu(In,Ga)Se_2[39], multi quantum wells and quantum dots solar cells.[40] A unique feature of this technique is the possibility to quantitatively measure the luminescence flux.[35, 36] Hyperspectral imaging, operating under uniform illumination of the device, allows to characterize the cell in a state close to the operation conditions, and was found free from a variety of artefacts occurring from analysis in a confocal configuration.[39] Local excitation systems have several major limitations that are surpassed by hyperspectral imaging. First of all the luminescence intensity is only available in arbitrary units, additionally all the optoelectronic parameters that are deduced from local excitation maps are altered by lateral carrier diffusion in proximity of the excitation spot. Finally, PL mapping alone provides insights solely about the active material, while the EL analysis gives important and complementary information on the electrical characteristics of the device. Within this perspective, hyperspectral imaging combines both methods in a quantitative manner. From the hyperspectral PL imaging and by using the generalized Planck's law, one can obtain absolute maps of the depth-averaged quasi-Fermi levels splitting ($\Delta\mu$), which determines the maximum achievable open circuit voltage (V_{oc}) of the solar cell.[41-44] Careful comparison with electrical measurement showed a consistent agreement between $\Delta\mu$ and V_{oc} on a variety of devices, within 20 meV.[41-44] On the other hand, by applying Rau's reciprocity relations on the hyperspectral EL maps, the spatial distribution of the photovoltage can be obtained.[45] Furthermore, the application of the generalized reciprocity relations allows to obtain maps of the charge carriers transport efficiency.[46]

In this manuscript, state-of-the-art p-i-n perovskite solar cells are analyzed by hyperspectral luminescence imaging. We investigated spatial fluctuations from few micron to the millimeter scale and compare samples having different hole blocking layers to understand the role of the front contact. To go further in the analysis we applied three different theories describing luminescence emission, i.e. spatially resolved absolute quasi-Fermi levels splitting from PL, from EL, as well as the carrier collection efficiency. We show that both photo- and electroluminescence are spatially not uniform, leading to a distribution of the quasi Fermi level splitting which strongly depends on the position in the device. Interestingly, only small deviations from the measured global V_{oc} are observed, which we ascribe to the small hysteresis observed in these solar cells. On the other hand, we also quantify and map the device spatial inhomogeneity by calculating the carrier transport efficiency. Surprisingly, we found small, yet non negligible areas where the photogenerated carrier collection efficiency is lower than 60%.

We show that this inefficient charge collection is most likely due to interfacial resistance fluctuations. Therefore, the performance of perovskite solar cells can be significantly improved by engineering the charge extraction and energy bands of the charge selective layers rather than by improving the quality of the perovskite absorber.

The architecture for the perovskite solar cells used in this study (Fig. 1a) consists of an indium tin oxide (ITO) coated glass slide, covered with a 80 nm thick poly(3,4-ethylenedioxythiophene):poly(styrene sulfonic acid) (PEDOT:PSS) layer and a thin (20 nm) poly[N,N’-bis(4-butylphenyl)-N,N’-bis(phenyl)benzidine] (polyTPD) film acting as the electron blocking layer. On top of this, the $MAPbI_3$ perovskite was thermally evaporated to a thickness of 500 nm using a previously described protocol.[14] Subsequently, a fullerene hole blocking layer was deposited on top of the perovskite absorber. In this study, we compared the behavior of a device with a solution processed [6,6]-phenyl C_{61}-butyric acid methylester (PCBM, 40 nm) film (device A) with that of one employing an evaporated C_{60} layer (also 40 nm, device B). The devices were completed with the evaporation of a Ba (10 nm) top electrode capped with Ag (100 nm). Details of the device preparation can be found in the Experimental section. Four cells were evaluated for each device configuration, showing virtually no difference in the observed performance. The EQE of both devices (Fig. 1b) is rather constant over the whole visible spectra, with a maximum of 85% at 600 nm, and shows the typical onset at 770 nm, corresponding to the perovskite band-to-band edge absorption. The current density (J) vs voltage (V) characteristic under dark and 1 Sun illumination are shown in Fig. 1c-b, and the corresponding extracted key device parameters are reported in Table 1. As expected from the EQE, the short circuit current densities (J_{sc}) are also high (19.90 mA/cm^2 for device A and 20.50 mA/cm^2 for device B), with the main difference among the two devices being the fill factor (FF, 0.687 for device A and

0.646 for device B), consequence of the use of different electron transport materials. The measured V_{oc} was found to be 1109 mV for device A and 1110 mV for device B, resulting in high power conversion efficiencies close to 15% (15.1% for device A and 14.70% for device B). Device A did not exhibit any substantial *J-V* hysteresis under the measurement conditions (scan speed of 0.35 V s^{-1}), while a weak hysteresis effect was observed for Device B. A comparison between the *J-V* curves under illumination and in the dark (Fig. 1c-d) suggests that both perovskite solar cells do have carrier collection issues to some extent. This interpretation originates from the relatively low FF for both samples as compared to the good diode characteristics (no evident resistance issues) observed in the dark. These phenomena will be investigated by using hyperspectral luminescence imaging.

Table 1 Performance parameters for perovskite solar cells as a function of the electron transport layer (ETL) and voltage scan direction

Device, ETL	Scan direction	J_{sc} (mA/cm^2)	V_{oc} (mV)	FF	PCE (%)
A, PCBM	Forward	19.90	1109	0.687	15.16
	Reverse	19.72	1106	0.679	14.81
B, C_{60}	Forward	20.50	1110	0.646	14.70
	Reverse	20.14	1107	0.615	13.71

Forward scan: from -0.2 V to 1.2 V. Reverse scan: from 1.2 V to -0.2 V. The scan speed was kept constant at 0.35 V s^{-1}.

The experimental setup consists of a hyperspectral imager coupled to an optical microscope which allows recording spectrally resolved images with a 2 nm spectral resolution and a 2 μm spatial resolution. The perovskite solar cell is homogeneously illuminated with a 532 nm laser, and for the detection of the luminescence images, a visible Si CCD camera is used. The spatial, spectral and absolute calibration procedures of the whole setup, are detailed elsewhere.[36]

As mentioned before, the hyperspectral imaging system quantitatively records luminescence maps, allowing the estimation of the quasi-Fermi levels splitting ($\Delta\mu$). This is achieved using the generalized Planck's law describing the luminescence spectrum of a material out of equilibrium.[42] By integration over the volume, the emission at a position *r* of the surface can be written as:

$$(1) \qquad \boldsymbol{j_r^L(E,r) = A(E,r)\frac{\Omega\cos\theta}{4\pi^3\hbar^3c^2}\frac{E^2}{exp\left(\frac{E-\Delta\mu(r)}{kT}\right)-1}} \quad ,$$

where $\boldsymbol{A(E,r)}$ is the absorption probability of an incident photon on the surface element, equal to its emissivity, by Kirchoff's law, Ω the solid angle of the emission, θ the angle of the emission relative to the surface normal, $\hbar$ is Planck's reduced constant, *c* is the speed of light, *E* is the photon energy and *kT* is the thermal energy. According to Rau's reciprocity relations and the Generalized Planck's law, the spectral shapes of the EL and PL spectra differ mainly because of a mismatch between the material's absorption *A(E)* and its *EQE(E)*. In our case the spectral shapes of PL and EL are identical (Fig. S6), which can only be true if *A(E)* is equal to the *EQE(E)*. Hence, the absorption $\boldsymbol{A(E,r)}$ can be approximated by the solar cell *EQE(E)*, within a factor close to unity. This assumption holds if the highest energy part of the calibrated PL spectra is used to estimate $\Delta\mu$. In any case, it only has a weak impact on the $\Delta\mu$ values whose fluctuations are logarithmically related to luminescence flux and absorption. In fact, a 20 % mismatch between *A(E)* and *EQE(E)* would only induce a variation of about *4 meV* in the $\Delta\mu$, as calculated from PL measurement following Eq. (1). This would still be within the global systematic error (± 20 meV) associated with the calculation and mapping of $\Delta\mu$, as reported elsewhere.[39] Equation (1) assumes that $\Delta\mu$ is constant throughout the semiconductor's depth.[41, 42] This assumptions is valid in view of the reports on long carrier diffusion lengths for perovskite solar cells, which is found to be larger than the active layer film thickness.[19, 20]. It is hence likely that traps or interface defects impact the $\Delta\mu$ throughout all of the depth. Hence, if the Fermi distribution is approximated by a Boltzmann distribution ($E - \Delta\mu_{eff} >> kT$), equation (1) can be re-written as:

$$(2) \qquad \boldsymbol{j_r^L\,(E,r) = A(E,r)\,\phi_{bb}(E,T)\,\mathbf{exp}\left(\frac{\Delta\mu(r)}{kT}\right)}\ ,$$

where $\boldsymbol{\phi_{bb}(E,T)}$ is the black body radiation. For the calculation and mapping of $\Delta\mu$ using equation (2), $\boldsymbol{EQE(E,r)}$ and T need to be determined. The temperature T can be determined from the generalized Planck's law applied to a luminescence flux $\boldsymbol{j_r^{PL,EL}}$, using the expression:

$$(3) \qquad \boldsymbol{kln\left(\frac{j_r^{PL,EL}}{A(E,r)E^2}\right) = \frac{\Delta\mu(r)}{T} - \frac{E}{T}}$$

By considering the high energy part of the spectrum, where the absorption does not vary significantly, the temperature T is obtained from the slope of the latter equation plotted against the photon energy. The fit in Fig. 2 yielded T = 297 K for device A and T = 303 K for device B. Note that the uncertainty in the temperature calculation is ± 20 K, meaning that the observed variations are negligible. Once the temperature is determined, from the constant term in the equation (3) the quasi-Fermi level splitting can be calculated. On the other hand, when analyzing

EL spectra, the diode voltage V can be obtained. In that case transport properties have to be taken into account. Reciprocity relations have been demonstrated between PV and LED devices.[23] Therefore the EL spectrum can be expressed using the following relation:

$$(4) \qquad \boldsymbol{j_r^{EL}\,(E,r) = EQE(E,r)\,\phi_{bb}(E,T)\,\exp\left(\frac{\Delta\mu(r)}{kT}\right)}$$

where in $\Delta\mu(\mathrm{r}) = qV(r)$, with $V(r)$ the local internal applied voltage and q the electronic charge. In order to measure the local voltage of the diode, an equivalent procedure as described above can be used.[47] The excitation power for all of the hyperspectral imaging experiments was kept below 1 Sun, allowing the characterization of the device under realistic operating conditions. This is an important criterion that is not often respected as usual PL characterizations, especially in confocal configuration, are obtained under several hundreds or even thousands Suns. For the PL experiments, the laser was tuned to match the electrically measured short circuit current $J_{sc} \sim 21$ mA/cm^2. As for the EL experiments, the same conditions were achieved with an applied bias of 1.15 V. We performed spectrally and spatially resolved luminescence imaging on both devices, obtaining absolutely calibrated PL and EL maps (photons/m/m^2/s). From these images, one can extract the emission spectrum from each pixel (Fig. 2a-b). EL and PL spectra exhibit similar shapes with equal emission maximum at 1.61 eV (770 nm), independently on the electron transport layer used.

By using the generalized Planck's law, maps of the quasi-Fermi levels splitting $\Delta\mu_{eff}$ can be extracted from the EL and PL hypercubes (Fig. 3). One can immediately notice the presence of circular spots with micrometric diameter that exhibit weak luminescence intensity and thus low quasi-Fermi level splitting. It is unlikely that these areas originates within the perovskite absorber. In fact, such spatial features are not directly related with the morphology/crystallinity of the perovskite layer, since the observed grain size is smaller than 200 nm (Fig. S1 in the Supporting Information). In this scenario, profound inhomogeneities in the perovskite would have a large impact on the electrical characteristic of the device (shunts, high current leakage, not seen here) that would strongly influence the efficiency and decrease the overall PL intensity. Hence the observed large inhomogeneities are most likely related to the deposition of the organic charge transport layers (PEDOT:PSS and polyTPD). These areas are potentially a damaging factor and lead to a lowering of the maximum achievable V_{oc}. Additionally, these areas contribute to the reduction of the carrier transport efficiency as will be demonstrated in the next section. In order to analyze the maps of the quasi-Fermi level splitting, the corresponding histograms representing the statistical spatial distribution of $\Delta\mu$ were obtained (Figure S2 in the Supplementary Information). Using a Gaussian distribution, the characteristic parameter from each hyperspectral analysis was extracted (the normalized Gaussian distributions are overlaid with the color bars in Fig. 3). For device A, and based on the map of $\Delta\mu$ extracted from the PL emission, we found a mean value $\boldsymbol{\Delta\mu_{PL}^{Center}}$= 1.017 eV with a full width at half maximum (FWHM) of 28.2 meV. This in very good agreement with the reference, global V_{oc} electrically measured under illumination with the 532 nm laser (1.015 V) and highlights the very good quality of the perovskite absorber. For device B, however, the PL imaging yields a mean value $\boldsymbol{\Delta\mu_{PL}^{Center}}$= 1.049 eV and a FWHM of 22.4 meV, which is slightly higher compared to the electrically measured V_{oc} of 1.002 V. This difference could originate from the particular area of the device under investigation, however full cell maps that will be described later appear to discard such effects. Most likely, the mismatch between $\Delta\mu$ and the measured V_{oc} is related to the hysteresis observed in the *J-V* characterization (Fig. 1d) and to a hindered charge extraction by interface potential barriers. In fact, discrepancies between the V_{oc} derived from PL experiments and that obtained from electrical measurements are indicators of the presence of interfacial charge trapping sites.[24, 25] Hence, the C_{60} hole blocking layer employed in device B might not be able to passivate the perovskite surface as efficiently as PCBM.[48, 49] For both devices the maximum spatial fluctuations of the quasi-Fermi level splitting is less than 50 meV (see Fig S3 in the Supplementary Information) and hence has a moderate impact on the global photovoltaic performance.[50-53] It is important to note that those fluctuations do not originate from spatial bandgap fluctuations, as demonstrated by the absence of spectral variations over the cell area.

The histograms of the spatially resolved $\Delta\mu$ obtained from EL were also determined (Figure S2 in the Supplementary Information). In the case of device A, the corresponding histogram plot is characterized by a mean value of 0.960 eV and a FWHM of 15.2 meV. For Device B, a very similar mean value of 0.963 eV with a FWHM of 13.1 meV is observed. In this case, both determined maximum $\boldsymbol{\Delta\mu_{EL}^{max}}$ are significantly lower (~190 meV) compared to the applied voltage (V_{app}=1.15 V). This mismatch points towards charge injection issues implying, due to the reciprocity relation, that the carrier collection is also limited. This observation is in agreement with the relatively low FF observed for both types of perovskite solar cells.

The theoretical work developed by Wong and Green provides an extension of Rau's reciprocity relations between PV (EQE) and LED operation (electroluminescence intensity).[46] This extension is based on the reformulation of Rau's work by including the terminal voltage and current, therefore extending its application to any device-operating point. The extended reciprocity relations take into account all the losses of elementary currents that occurs while reaching the terminal, with an efficiency f_T given by:

(5) $$\boldsymbol{f_T}(\boldsymbol{x},\boldsymbol{y}) = \frac{\partial \boldsymbol{I}}{\partial \boldsymbol{I_L}(\boldsymbol{x},\boldsymbol{y})}_{\partial \boldsymbol{V_T}=\boldsymbol{0}} = \frac{\partial \boldsymbol{V}(\boldsymbol{x},\boldsymbol{y})}{\partial \boldsymbol{V_T}}_{\partial \boldsymbol{I_L}=\boldsymbol{0}}$$

where I and V_T are the terminal current and voltage, $I_L(x,y)$ the local light induced current collected at the junction, and $V(x,y)$ the local diode voltage. This definition of a generalized relation connects the injection of carriers in the dark to the extraction of carriers under illumination. Hence collection efficiency maps can be experimentally accessible by using Eq. (4), which relates the local EL intensity to the local voltage and EQE values. In fact, one can determine the current transport efficiency by differentiating the electroluminescence emission:[45]

(6) $$\boldsymbol{f_T}(\boldsymbol{x},\boldsymbol{y}) = \frac{\partial \boldsymbol{ln\phi_{em}}(\boldsymbol{x},\boldsymbol{y})}{\partial\left(\frac{\boldsymbol{qV_T}}{\boldsymbol{KT}}\right)}$$

where $\boldsymbol{\phi_{EL}}(\boldsymbol{x},\boldsymbol{y})$ is the EL map. Therefore, depending on the bias we apply, f_T variations could arise from a bias dependence of the EQE (i.e. carrier collection function) or from local voltage variations. This is further discussed below based on our experimental results. Two EL images were acquired by applying voltages of 1.15 V and 1.16 V and, by applying equation (6), maps of the current transport efficiency were obtained for both types of devices (Fig. 4). The current transport efficiency exhibits spatial variations at the micron scale (Fig. 4 a-b) which are similar in size and appearance to those previously observed for the quasi-Fermi level splitting obtained from both the PL and EL (Fig. 3). The corresponding histograms are shown in Fig. S3 in the Supplementary Information, and their deconvolutions are overlaid with the color bars in Fig. 4. In device A, f_T is broad and centered at 0.5, with low (0.27) and high (0.80) narrow components originating from the small regions visible in Fig. 4a. The current transport efficiency for device B (Fig. 4b) shows substantial inhomogeneities on a much larger scale, with f_T being dominated by a relatively low (0.42) and a high (0.78) broad components. For both devices, the spatial distribution of f_T shows areas approaching unity, indicating full collection of the photogenerated charge carriers, and small portions of the image where all charge carriers are essentially lost. It is important to point out, however, that in order to obtain a sufficient EL signal and respect the standard 1 Sun operation conditions, the applied voltage in our experiments is only slightly above the V_{oc} obtained under 1 Sun illumination. This choice unavoidably underestimates the collection efficiency. In fact, at short circuit the carrier collection efficiency is much higher, as evidenced by the measured J_{sc} of about 20 mA/cm^2 (Fig. 1c-d). According to these maps our perovskite solar cells, in spite of their high power efficiency, exhibit areas with substantially limited current transport efficiency. This observation is in good agreement with the low fill factor observed for the devices studied here. Our investigation has so far focused on the hyperspectral imaging of the luminescence emitted from an area that is small compared to the total device area (6 mm^2). In the following section the results from the analysis on the full device area is presented. As in the case of the micro-scale analysis, the EL images used to calculate f_T were taken at 1.15 V and 1.16 V applied bias. By examining the full scale f_T maps for both perovskite devices (Fig. 4 c-d), strong spatial inhomogeneity with millimeter variations can be observed. These fluctuations are of the same order of magnitude compared to those observed at the micrometric scale. The spatial distributions of the carrier transport efficiency shows the presence of multiple areas within the full device, each being dominated by different values of f_T (see histograms in Fig. S3 in the Supplementary Information, and their deconvolutions which are overlaid with the color bars in Fig. 4). For device A (Fig. 4c), only a few regions have a low transport efficiency (< 0.2), while the distribution of f_T shows two main features at 0.43 and 0.64. The device using a C_{60} electron transport layer (device B) is characterized by a somewhat narrower distribution in the transport efficiency (Fig 4d), with a main peak at 0.52 and a long shoulder at higher values of f_T, where the current transport is enhanced. Interestingly, areas exhibiting an almost complete collection of the photogenerated charges are present at the edges of the active area for both devices (red areas in Fig. 4c-d). Such edge effects are ascribed to small thickness variation due to the edge of the underlying patterned ITO electrode, which defines the active area of the solar cell. More importantly, these figures translate into a large loss of the photogenerated charge carriers even in high efficiency perovskite solar cells as those presented here. Moreover, carrier collection issues seem to be present at both local and global scale.

The origin of not efficient carrier transport can come either from the collection in the diode (classically called f_c collection function) or rather from a lateral transport within the electrodes.[46] In case of the first hypothesis, one would expect a strong voltage dependence of the EQE values, consequence of the presence of traps or of a limited mobility in the absorber. As this is not observed, (Fig. S5 in Supporting Information), the collection function appears not to be the main reason for the observed inefficient charge transport. Additionally, in such a scenario, one would also expect a mismatch between EL and PL spectra, as the former reflects the $EQE(E,r)$ and the latter reflects the absorption $A(E,r)$, which is also not observed here (Fig. 2 and Fig S6 in Supplementary information). Finally, $EQE(E,r)$ variations indicate fluctuations of internal diode voltages[45] and thus spatial fluctuations of local series resistances (as opposed to lateral spreading resistance). Since similar spatial variations are observed for sample A and B, the origin of such losses possibly originates from the front (ITO/PEDOT/polyTPD) rather than the back contact (fullerene). Although it deserves more investigation, this could also indicate the presence of an energy barrier (as mentioned before), as we see small variations of the *EQE(V)* in the blue region of the spectrum. Regarding this phenomena and considering that the EQE(V) is a global measurement, one cannot a priori exclude a different behavior on a more local scale. Nevertheless, as the observed global tendency is not voltage dependent, a different local behavior would not influence the overall parameters. The second hypothesis implying lateral carrier transport issues as the cause for the low carrier collection efficiency would lead to a monotonous variations of the carrier collection function. This is not the case at the microscale but it might be responsible for larger fluctuations observed on the complete cell area. For device A, a f_T gradient is seen in the x direction only, while a gradient in both x and y directions is observed for device B. As the front contact is common to both devices (ITO/PEDOT:PSS/polyTPD), its lateral conductivity plays a role in the f_T spatial variations (x direction). On the other hand, the back side with the PCBM layer seems to have a higher lateral carrier extraction efficiency compared to the device using C_{60}. In fact for device B we observe f_T variations also the y-direction. Although this effect has no impact under 1 sun working conditions (both devices having similar properties), it will be more relevant for larger devices. These phenomena would also explain why only few efficient large area perovskite cells have been reported so far, since the fill factor is normally lower than in the equivalent smaller area cells.[54]

In summary, we have investigated efficient p-i-n hybrid perovskite solar cells through luminescence hyperspectral imaging. The small mismatch between the electrically measured V_{oc} and the optically (from both photoluminescence and electroluminescence) deduced quasi-Fermi level splitting is indicative of the high quality of the perovskite absorber. Yet the spatially resolved analysis identified profound inhomogeneities in this novel type of devices. These spatial inhomogeneities appear to be related with problems with carrier extraction leading to the limited fill factor of the cells. This hypothesis is supported by the dispersion of the spatially resolved carrier transport efficiency function, which identifies areas of the cell with severely hindered charge transport. We ascribe these losses first to local fluctuations of interface series resistance and, with lower impact, to inefficient lateral transport. The origin of the inhomogeneities observed here is not yet clear, but its understanding would allow to significantly enhance the performance of these already efficient photovoltaic devices. This work also demonstrated that hyperspectral luminescence imaging is a powerful tool to investigate the lateral variations of novel devices such as hybrid perovskite solar cells.

Experimental

Perovskite solar cell fabrication. ITO-coated glass substrate were cleaned with soap, water and isopropanol in an ultrasonic bath, followed by O_2 plasma treatment. PEDOT:PSS was spin-coated on top and annealed at 150 ºC for 15 minutes. PolyTPD was spin-coated from a chlorobenzene solution (7 mg ml^{-1}), obtaining a 20 nm thick layer. Substrates were transferred to a vacuum chamber integrated into a nitrogen-filled glovebox and evacuated to a pressure of $1\cdot10^{-6}$ mbar. Two ceramic crucibles containing MAI and PbI_2 were heated at 70ºC and 250ºC, respectively. The film thickness was controlled by the PbI_2 evaporation rate (0.5 A s^{-1}). After evaporation of a 500 nm thick $MAPbI_3$ perovskite, a 40 nm film of C60 was evaporated on top without breaking the vacuum. Alternatively, a 40 nm thick PCBM layer was spin-coated from a chlorobenzene solution (20 mg ml^{-1}) in ambient conditions. The devices were completed by thermal evaporation of the top metal electrode under a base pressure of $1\cdot10^{-6}$ mbar (10nm Ba/100 nm Ag).

Solar cells characterization and hyperspectral imaging. EQE measurements were performed using a white light halogen lamp (calibrated on a reference Si solar cell) in combination with interference filters (MiniSun simulator by ECN, the Netherlands). Current density-voltage (*J-V*) characteristics were measured using a Keithley 2400 source measure unit with and without illumination. The light source was a 10500 solar simulator by Abet Technologies. Before each measurement, the exact light intensity was determined using a calibrated Si reference solar cell. The setup for the hyperspectral luminescence imaging consists of a hyperspectral imager from Photon etc. coupled to an optical microscope with a 50x objective and a numerical aperture of 0.8. An optical setup based on a Köhler system provided the homogeneous illumination of the perovskite devices. The global illumination inhomogeneity is found to be lower than 9%.

Acknowledgements

This work has been supported by the Spanish Ministry of Economy and Competitiveness (MINECO) via the Unidad de Excelencia María de Maeztu MDM-2015-0538 and MAT2014-55200, PCIN-2015-255 and the Generalitat Valenciana (Prometeo/2012/053). C. M., and M.S. thank the MINECO for their pre- and post-doctoral (JdC) contracts. G.E.H. would like to thank the ANRT for financing the ongoing PhD thesis under the CIFRE convention N° 923/2013. The authors acknowledge Photon Etc (M. Verhaegen and L.-I. Dion-Bertrand) for fruitful discussions and technical assistance.

References

1. A. Kojima, K. Teshima, Y. Shirai and T. Miyasaka, *Journal of the American Chemical Society*, 2009, **131**, 6050-6051.

2. M. M. Lee, J. Teuscher, T. Miyasaka, T. N. Murakami and H. J. Snaith, *Science*, 2012, **338**, 643-647.
3. J. Burschka, N. Pellet, S.-J. Moon, R. Humphry-Baker, P. Gao, M. K. Nazeeruddin and M. Gratzel, *Nature*, 2013, **499**, 316-319.
4. N. J. Jeon, J. H. Noh, Y. C. Kim, W. S. Yang, S. Ryu and S. I. Seok, *Nat Mater*, 2014, **13**, 897-903.
5. H. Zhou, Q. Chen, G. Li, S. Luo, T.-b. Song, H.-S. Duan, Z. Hong, J. You, Y. Liu and Y. Yang, *Science*, 2014, **345**, 542-546.
6. W. S. Yang, J. H. Noh, N. J. Jeon, Y. C. Kim, S. Ryu, J. Seo and S. I. Seok, *Science*, 2015, DOI: 10.1126/science.aaa9272.
7. P. Gao, M. Gratzel and M. K. Nazeeruddin, *Energy & Environmental Science*, 2014, **7**, 2448-2463.
8. M. Gratzel, *Nat Mater*, 2014, **13**, 838-842.
9. S. D. Stranks and H. J. Snaith, *Nat Nano*, 2015, **10**, 391-402.
10. J. Berry, T. Buonassisi, D. A. Egger, G. Hodes, L. Kronik, Y.-L. Loo, I. Lubomirsky, S. R. Marder, Y. Mastai, J. S. Miller, D. B. Mitzi, Y. Paz, A. M. Rappe, I. Riess, B. Rybtchinski, O. Stafsudd, V. Stevanovic, M. F. Toney, D. Zitoun, A. Kahn, D. Ginley and D. Cahen, *Advanced Materials*, 2015, **27**, 5102-5112.
11. M. A. Green, K. Emery, Y. Hishikawa, W. Warta and E. D. Dunlop, *Progress in Photovoltaics: Research and Applications*, 2015, **23**, 805-812.
12. D. Bi, W. Tress, M. I. Dar, P. Gao, J. Luo, C. Renevier, K. Schenk, A. Abate, F. Giordano, J.-P. Correa Baena, J.-D. Decoppet, S. M. Zakeeruddin, M. K. Nazeeruddin, M. Grätzel and A. Hagfeldt, *Science Advances*, 2016, **2**.
13. M. Liu, M. B. Johnston and H. J. Snaith, *Nature*, 2013, **501**, 395-398.
14. O. Malinkiewicz, A. Yella, Y. H. Lee, G. M. Espallargas, M. Graetzel, M. K. Nazeeruddin and H. J. Bolink, *Nat Photon*, 2014, **8**, 128-132.
15. Q. Lin, A. Armin, R. C. R. Nagiri, P. L. Burn and P. Meredith, *Nat Photon*, 2015, **9**, 106-112.
16. W. Nie, H. Tsai, R. Asadpour, J.-C. Blancon, A. J. Neukirch, G. Gupta, J. J. Crochet, M. Chhowalla, S. Tretiak, M. A. Alam, H.-L. Wang and A. D. Mohite, *Science*, 2015, **347**, 522-525.
17. D. Shi, V. Adinolfi, R. Comin, M. Yuan, E. Alarousu, A. Buin, Y. Chen, S. Hoogland, A. Rothenberger, K. Katsiev, Y. Losovyj, X. Zhang, P. A. Dowben, O. F. Mohammed, E. H. Sargent and O. M. Bakr, *Science*, 2015, **347**, 519-522.
18. Q. Dong, Y. Fang, Y. Shao, P. Mulligan, J. Qiu, L. Cao and J. Huang, *Science*, 2015, **347**, 967-970.
19. G. Xing, N. Mathews, S. Sun, S. S. Lim, Y. M. Lam, M. Grätzel, S. Mhaisalkar and T. C. Sum, *Science*, 2013, **342**, 344-347.
20. S. D. Stranks, G. E. Eperon, G. Grancini, C. Menelaou, M. J. P. Alcocer, T. Leijtens, L. M. Herz, A. Petrozza and H. J. Snaith, *Science*, 2013, **342**, 341-344.
21. C. Wehrenfennig, G. E. Eperon, M. B. Johnston, H. J. Snaith and L. M. Herz, *Advanced Materials*, 2014, **26**, 1584-1589.
22. C. S. Ponseca, T. J. Savenije, M. Abdellah, K. Zheng, A. Yartsev, T. Pascher, T. Harlang, P. Chabera, T. Pullerits, A. Stepanov, J.-P. Wolf and V. Sundström, *Journal of the American Chemical Society*, 2014, **136**, 5189-5192.
23. U. Rau, *Physical Review B - Condensed Matter and Materials Physics*, 2007, **76**.
24. K. Tvingstedt, O. Malinkiewicz, A. Baumann, C. Deibel, H. J. Snaith, V. Dyakonov and H. J. Bolink, *Sci. Rep.*, 2014, **4**, 6071.
25. W. Tress, N. Marinova, O. Inganäs, M. K. Nazeeruddin, S. M. Zakeeruddin and M. Graetzel, *Advanced Energy Materials*, 2015, **5**, n/a-n/a.
26. D. W. deQuilettes, S. M. Vorpahl, S. D. Stranks, H. Nagaoka, G. E. Eperon, M. E. Ziffer, H. J. Snaith and D. S. Ginger, *Science*, 2015, **348**, 683-686.

27. M. J. Simpson, B. Doughty, B. Yang, K. Xiao and Y.-Z. Ma, *The Journal of Physical Chemistry Letters*, 2015, **6**, 3041-3047.
28. Z. Hameiri, A. Mahboubi Soufiani, M. K. Juhl, L. Jiang, F. Huang, Y.-B. Cheng, H. Kampwerth, J. W. Weber, M. A. Green and T. Trupke, *Progress in Photovoltaics: Research and Applications*, 2015, **23**, 1697-1705.
29. X. Wen, R. Sheng, A. W. Y. Ho-Baillie, A. Benda, S. Woo, Q. Ma, S. Huang and M. A. Green, *The Journal of Physical Chemistry Letters*, 2014, **5**, 3849-3853.
30. C. G. Bischak, E. M. Sanehira, J. T. Precht, J. M. Luther and N. S. Ginsberg, *Nano Letters*, 2015, **15**, 4799-4807.
31. Z. Guo, J. S. Manser, Y. Wan, P. V. Kamat and L. Huang, *Nat Commun*, 2015, **6**.
32. Y. Tian, M. Peter, E. Unger, M. Abdellah, K. Zheng, T. Pullerits, A. Yartsev, V. Sundstrom and I. G. Scheblykin, *Physical Chemistry Chemical Physics*, 2015, **17**, 24978-24987.
33. M. Vrućinić, C. Matthiesen, A. Sadhanala, G. Divitini, S. Cacovich, S. E. Dutton, C. Ducati, M. Atatüre, H. Snaith, R. H. Friend, H. Sirringhaus and F. Deschler, *Advanced Science*, 2015, **2**, n/a-n/a.
34. J. S. Yun, A. Ho-Baillie, S. Huang, S. H. Woo, Y. Heo, J. Seidel, F. Huang, Y.-B. Cheng and M. A. Green, *The Journal of Physical Chemistry Letters*, 2015, **6**, 875-880.
35. A. Delamarre, L. Lombez and J.-F. Guillemoles, *Applied Physics Letters*, 2012, **100**, 131108.
36. A. Delamarre, L. Lombez and J. F. Guillemoles, *PHOTOE*, 2012, **2**.
37. E. Olsen and A. S. Flø, *Applied Physics Letters*, 2011, **99**.
38. M. P. Peloso, J. Sern Lew, T. Trupke, M. Peters, R. Utama and A. G. Aberle, *Applied Physics Letters*, 2011, **99**.
39. A. Delamarre, M. Paire, J.-F. Guillemoles and L. Lombez, *Progress in Photovoltaics: Research and Applications*, 2014, DOI: 10.1002/pip.2555, n/a-n/a.
40. P. Rale, A. Delamarre, G. El-Hajje, R. Tamaki, K. Watanabe, Y. Shoji, Y. Okada, M. Sugiyama, L. Lombez and J.-F. Guillemoles, *PHOTOE*, 2015, **5**, 053092-053092.
41. G. Lasher and F. Stern, *Physical Review*, 1964, **133**, A553-A563.
42. P. Wurfel, *Journal of Physics C: Solid State Physics*, 1982, **15**, 3967-3985.
43. B. Feuerbacher and P. Wurfel, *Journal of Physics: Condensed Matter*, 1990, **2**, 3803-3810.
44. K. Schick, E. Daub, S. Finkbeiner and P. Würfel, *Applied Physics A Solids and Surfaces*, 1992, **54**, 109-114.
45. U. Rau, *Physical Review B*, 2007, **76**, 085303.
46. J. Wong and M. A. Green, *Physical Review B*, 2012, **85**, 235205.
47. T. Kirchartz, U. Rau, M. Kurth, J. Mattheis and J. H. Werner, *Thin Solid Films*, 2007, **515**, 6238-6242.
48. Y. Shao, Z. Xiao, C. Bi, Y. Yuan and J. Huang, *Nat Commun*, 2014, **5**.
49. J. Xu, A. Buin, A. H. Ip, W. Li, O. Voznyy, R. Comin, M. Yuan, S. Jeon, Z. Ning, J. J. McDowell, P. Kanjanaboos, J.-P. Sun, X. Lan, L. N. Quan, D. H. Kim, I. G. Hill, P. Maksymovych and E. H. Sargent, *Nat Commun*, 2015, **6**.
50. U. Rau, P. O. Grabitz and J. H. Werner, *Applied Physics Letters*, 2004, **85**, 6010-6012.
51. G. H. Bauer and L. Gütay, *Thin Solid Films*, 2007, **515**, 6127-6131.
52. E. Edri, S. Kirmayer, S. Mukhopadhyay, K. Gartsman, G. Hodes and D. Cahen, *Nat Commun*, 2014, **5**.
53. V. W. Bergmann, S. A. L. Weber, F. Javier Ramos, M. K. Nazeeruddin, M. Grätzel, D. Li, A. L. Domanski, I. Lieberwirth, S. Ahmad and R. Berger, *Nat Commun*, 2014, **5**.
54. O. Malinkiewicz, C. Roldán-Carmona, A. Soriano, E. Bandiello, L. Camacho, M. K. Nazeeruddin and H. J. Bolink, *Advanced Energy Materials*, 2014, **4**, 1400345.

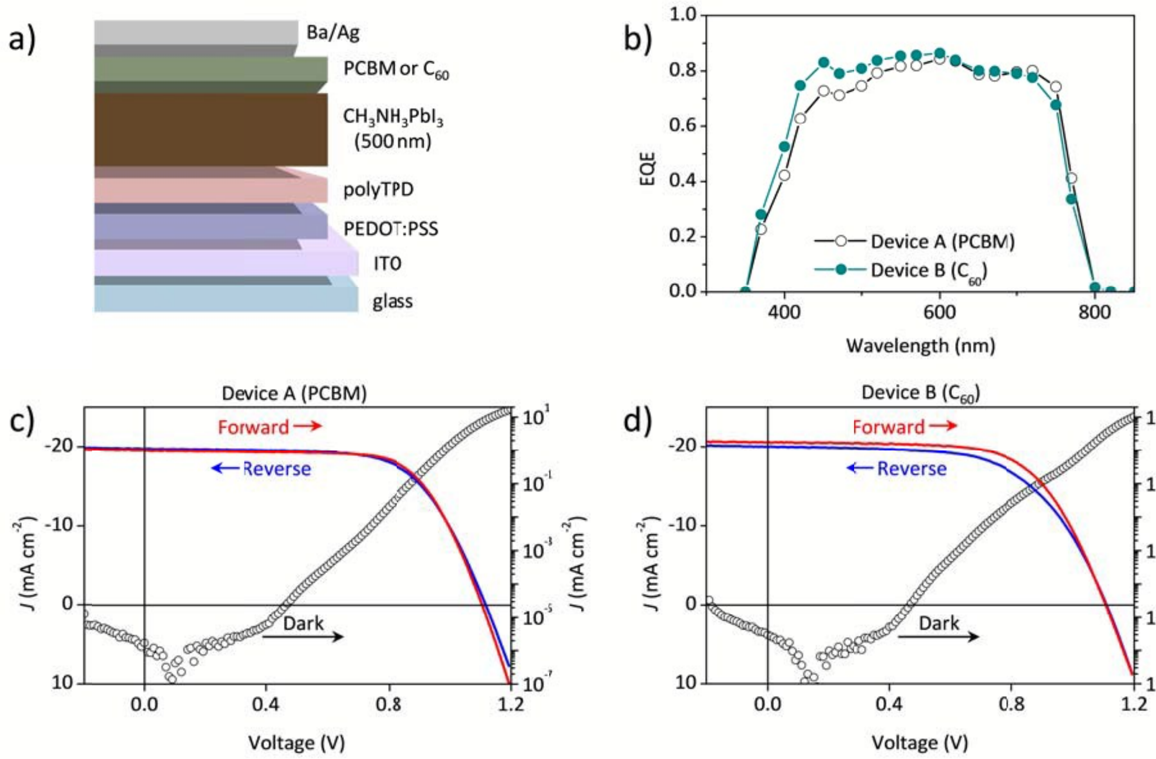

Fig. 1 (a) Structure schematics for the perovskite cells used. (b) EQE and *J*-*V* characteristic under illumination (lines, left axis) and in the dark (symbols, right axis) for devices employing PCBM (c) and C_{60} (d) as the electron transport layer.

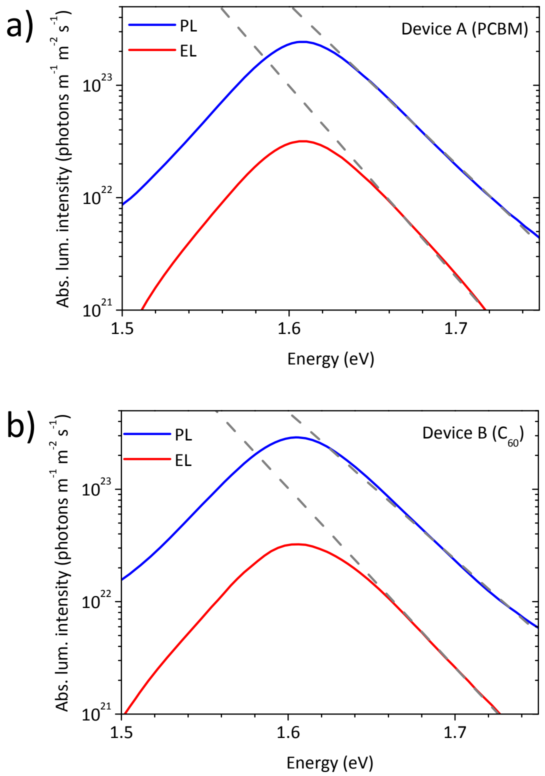

Fig. 2 (a) Photoluminescence (blue) and electroluminescence (red) spectra for device A, using PCBM, and for (b) device B, using C_{60} as the electron transport layer. The linear fit of the high energy tail of the spectra is used to calculate the temperature *T* following equation (3).

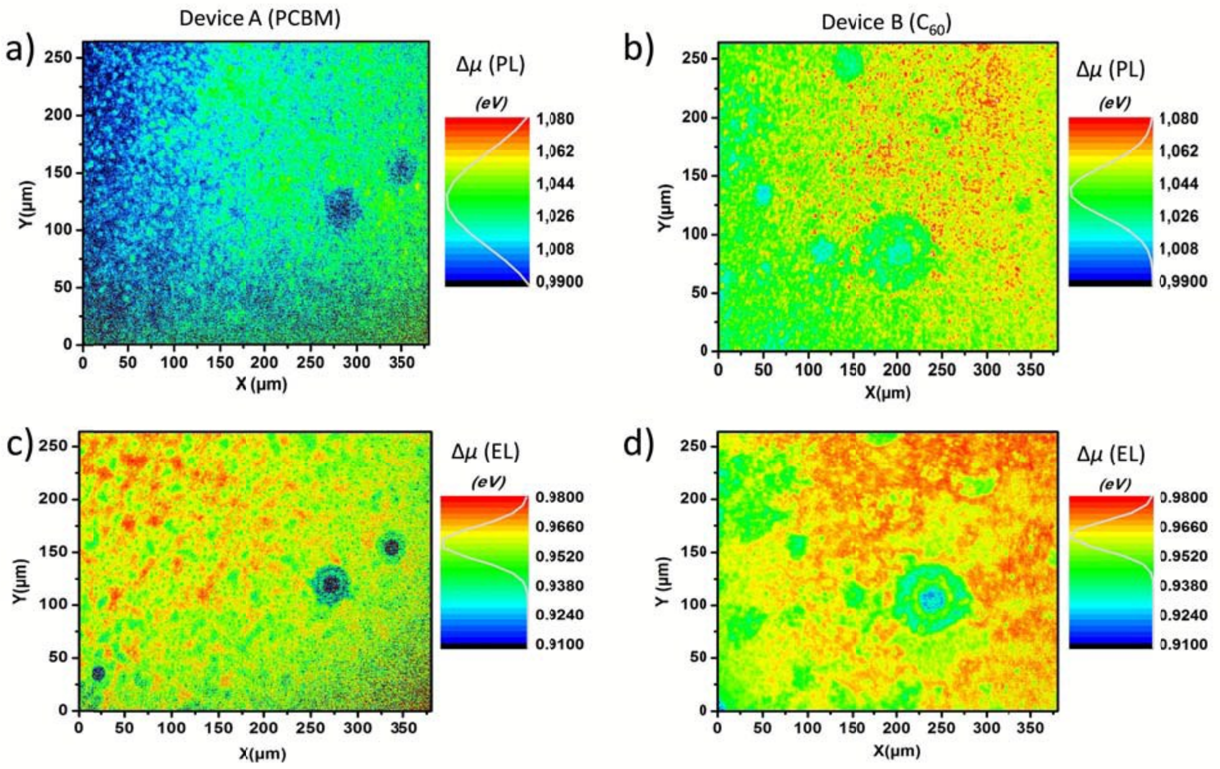

Fig. 3 (a) Absolute mapping of the quasi-Fermi level splitting derived from photoluminescence (a, b, top) and electroluminescence (c, d, bottom), for perovskite solar cells using PCBM (left, device A) or C_{60} (right, device B) as the ETL. The Gaussian distribution of the signal has been overlaid with the color scale as a guide to the eye.

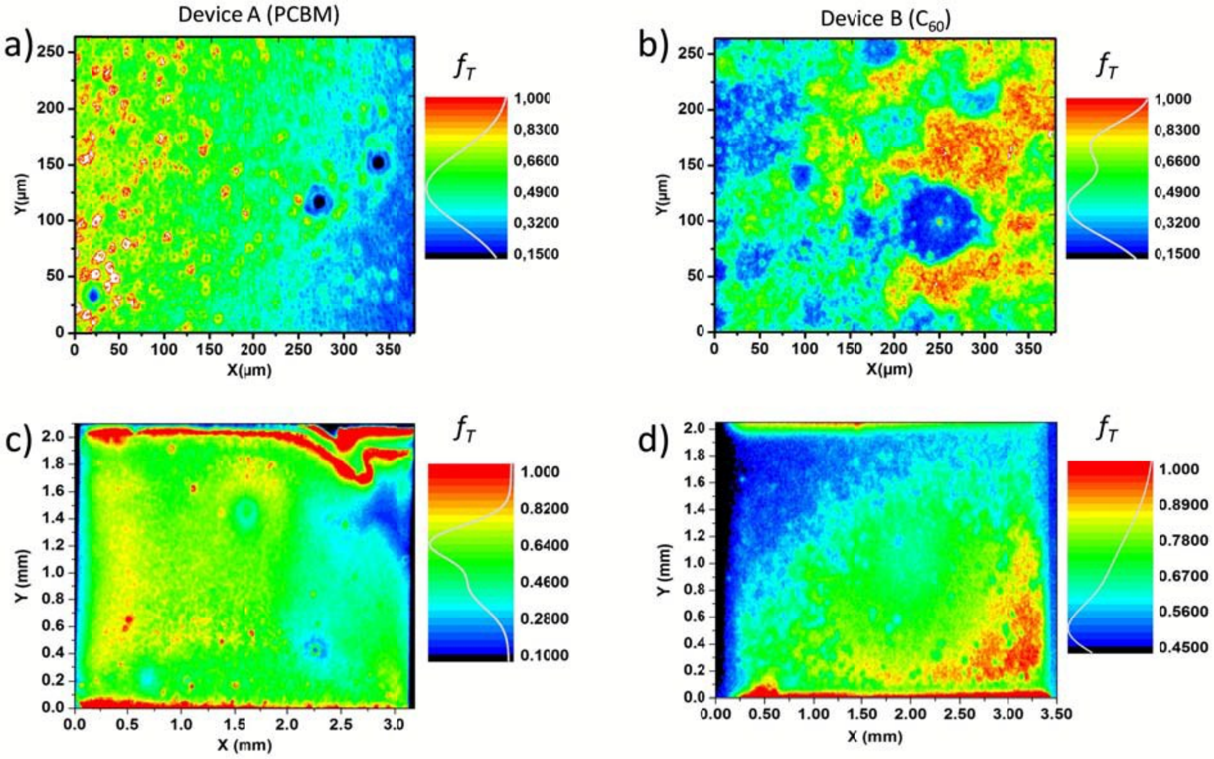

Fig. 4 Mapping of the current transport efficiency f_T obtained by applying equation (5) to two EL hyperspectral images taken at 1.15 V and 1.16 V applied bias. f_T mapping was performed at the microscale (top) and at the whole device level (bottom) for perovskite solar cells using PCBM (a, c, device A) or C_{60} (b, d, device B) as the ETL. The interpolation of the signal distribution has been overlaid with the color scale as a guide to the eye.

High efficiency solar cells employing inexpensive hybrid perovskite absorbers are widely studied as a potential future energy source. Investigating the PL and EL properties of perovskites is a valuable tool to unveil their properties and limitations. Interestingly, many studies have highlighted a rather inhomogeneous spatial distribution of the luminescence, in contrast with the very high efficiencies reported. Most of those studies used local excitation at very high intensity and, importantly, the luminescence has been observed only qualitatively. In this study, we use hyperspectral luminescence imaging to study planar p-i-n solar cells employing vacuum deposited $CH_3NH_3PbI_3$ perovskite absorbers. Through this technique, it is possible to quantify the number of photons emitted from every point of the device at every wavelength. We investigated spatial fluctuations from few micron to the millimeter scale and show that both photo- and electroluminescence are spatially not uniform, leading to a distribution of the quasi Fermi level splitting which strongly depends on the position in the device. We also map the carrier transport efficiency, finding areas where the photogenerated carrier collection efficiency is lower than 60%. We show that this inefficient charge collection is most likely due to interfacial resistance fluctuations. This work is relevant for perovskite and organic based opto-electronic devices.